






The intrinsic alignment of galaxy clusters and impact of projection effects

Jingjing Shi ^{1,2}★ Tomomi Sunayama,^{3,4} Toshiki Kurita ¹, Masahiro Takada,^{1,2} Sunao Sugiyama,^{1,2} Rachel Mandelbaum ⁵, Hironao Miyatake ³, Surhud More ^{6,1}, Takahiro Nishimichi^{8,7,1} and Harry Johnston⁹

¹*Kavli Institute for the Physics and Mathematics of the Universe (WPI), The University of Tokyo Institutes for Advanced Study (UTIAS), The University of Tokyo, 5-1-5 Kashiwanoha, Kashiwa-shi, Chiba 277-8583, Japan*

²*Center for Data-Driven Discovery (CD3), Kavli IPMU (WPI), UTIAS, The University of Tokyo, Kashiwa, Chiba 277-8583, Japan*

³*Kobayashi-Maskawa Institute for the Origin of Particles and the Universe (KMI), Nagoya University, Nagoya 464-8602, Japan*

⁴*Department of Astronomy and Steward Observatory, University of Arizona, 933 N Cherry Ave, Tucson, AZ 85719, USA*

⁵*McWilliams Center for Cosmology, Department of Physics, Carnegie Mellon University, Pittsburgh, PA 15213, USA*

⁶*The Inter-University Centre for Astronomy and Astrophysics, Post bag 4, Ganeshkhind, Pune 411007, India*

⁷*Center for Gravitational Physics and Quantum Information, Yukawa Institute for Theoretical Physics, Kyoto University, Kyoto 606-8502, Japan*

⁸*Department of Astrophysics and Atmospheric Sciences, Faculty of Science, Kyoto Sangyo University, Kyoto 603-8555, Japan*

⁹*Institute for Theoretical Physics, Utrecht University, Princetonplein 5, NL-3584 CE Utrecht, the Netherlands*

Accepted 2024 January 5. Received 2023 December 30; in original form 2023 June 16

ABSTRACT

Galaxy clusters, being the most massive objects in the Universe, exhibit the strongest alignment with the large-scale structure. However, mis-identification of members due to projection effects from the large-scale structure can occur. We studied the impact of projection effects on the measurement of the intrinsic alignment of galaxy clusters, using galaxy cluster mock catalogues. Our findings showed that projection effects result in a decrease of the large-scale intrinsic alignment signal of the cluster and produce a bump at $r_p \sim 1 h^{-1}$ Mpc, most likely due to interlopers and missed member galaxies. This decrease in signal explains the observed similar alignment strength between bright central galaxies and clusters in the SDSS redMaPPer cluster catalogue. The projection effect and cluster intrinsic alignment signal are coupled, with clusters having lower fractions of missing members or having higher fraction of interlopers exhibiting higher alignment signals in their projected shapes. We aim to use these findings to determine the impact of projection effects on galaxy cluster cosmology in future studies.

Key words: galaxies: clusters: general – large-scale structure of Universe – cosmology: observations – cosmology: theory.

1 INTRODUCTION

Galaxy clusters are a major probe of dark energy (Weinberg et al. 2013). Their abundance and time evolution are sensitive to the growth of structure in the Universe, since they form from rare highest peaks of the initial density field. Cluster cosmology is a major science of many surveys, including Hyper Suprime-Cam survey (Aihara et al. 2018, 2022),¹ the Dark Energy Survey (Dark Energy Survey Collaboration et al. 2016),² the Kilo Degree Survey (Kuijken et al. 2015),³ the Rubin Observatory Legacy Survey of Space and Time (LSST Science Collaboration et al. 2009),⁴ Euclid (Laureijs et al. 2011),⁵ and the *Nancy Grace Roman Telescope* (Bailey et al. 2023).⁶

Cluster shapes are triaxial, originating from the anisotropic matter field and accretion. As a result, cluster shapes are expected to

align with the matter field, i.e. intrinsic alignment (IA) (see review papers by Joachimi et al. 2015; Kiessling et al. 2015; Kirk et al. 2015; Troxel & Ishak 2015). IA are distinct from the alignments of galaxy shapes that originate from gravitational lensing by foreground attractors. The IA signal has been observed for massive red galaxies (Okumura, Jing & Li 2009; Singh, Mandelbaum & More 2015), but no clear detection has been claimed for blue galaxies (Mandelbaum et al. 2011; Yao et al. 2020). The alignment of galaxy clusters has also been detected (Smargon et al. 2012). van Uitert & Joachimi (2017) studied the cluster shape–density correlation using redMaPPer clusters from Sloan Digital Sky Survey-Data Release 8 (SDSS DR8), finding a higher IA amplitude of galaxy clusters than luminous red galaxies (LRGs). As clusters are the most massive bound structures, studies on cluster shapes offer the unique opportunity to yield insight into dark matter halo shapes (Evans & Bridle 2009; Oguri et al. 2010; Shin et al. 2018; Gonzalez et al. 2022).

However, the IA amplitude of galaxy clusters is found to be lower than predictions from numerical N -body simulations based on Λ cold dark matter (Λ CDM) cosmology. Smargon et al. (2012) discussed various systematic observational uncertainties that may have caused this discrepancy, including photometric redshift error, cluster centroiding error, uncertainty in cluster shape estimation

* E-mail: jingssrs1989@gmail.com

¹<https://hsc.mtk.nao.ac.jp/ssp/>

²<https://www.darkenergysurvey.org/>

³<https://kids.strw.leidenuniv.nl/>

⁴<https://www.lsst.org/>

⁵<https://www.euclid-ec.org/>

⁶<https://roman.gsfc.nasa.gov/>

using a limited subsample of galaxy members, and inclusion of spherical clusters. However, one of the major systematics for optically identified clusters, the so-called ‘projection effect’, has not been properly discussed for measurement of IA for galaxy clusters.

Projection effects refer to the fact that interloper galaxies along the line of sight (LOS) are mistakenly identified as members of galaxy clusters (van Haarlem, Frenk & White 1997; Cohn et al. 2007). This is a major systematics for optical clusters whose mass proxy is a number of member galaxies (called richness). It can also boost cluster lensing and clustering signals on large scales, since clusters with a filamentary structure aligned with the LOS direction are preferentially identified by optical cluster finders, which typically detect clusters using red galaxy overdensities in photometric catalogues (Osato et al. 2018; Sunayama et al. 2020; Sunayama 2023). To obtain unbiased cosmological constraints using galaxy clusters, the projection effect has to be corrected or modelled accurately (Costanzi et al. 2019; To et al. 2021; Park et al. 2023).

In this work, we will study the impact of projection effects on measurements of cluster IA with the aim to understand the measured IA of the most massive objects. We also search for new perspectives on projection effects and possible ways to mitigate the impacts on cluster observables. We found that the projection effects can largely explain the lower signal of observed cluster IA compared to that of simulated dark matter haloes.

The structure of the paper is organized as follows. In Section 2, we introduce our methodology for measuring the correlation function and modelling the signals. In Section 3, we introduce the observational data and mock simulation used in this paper. The results on measured IA in observation and mocks – including the impact of projection effects – are presented in Section 4 and Section 5. In Section 6, we summarize our results.

2 METHODOLOGY – LINEAR ALIGNMENT MODEL

In this section we briefly describe the leading theory of IA, i.e. the linear alignment model (Catelan, Kamionkowski & Blandford 2001; Hirata & Seljak 2004), and then define the model to use for the comparison with the IA measurements of the redMaPPer clusters.

The linear alignment model predicts that the intrinsic shape of dark matter haloes, and galaxy clusters in this paper, is determined by the gravitational tidal field at the time of formation of the halo or galaxy cluster. That is, the intrinsic ‘shear’, which characterizes the shape of galaxy cluster, is given as

$$\langle \gamma_1, \gamma_2 \rangle = -\frac{C_1}{4\pi G} (\partial_x^2 - \partial_y^2, \partial_x \partial_y) \Phi_p, \quad (1)$$

where Φ_p is the primordial gravitational field and C_1 is a constant. Here we take the (x, y) coordinates to be on the 2D plane perpendicular to the LOS direction. Throughout this paper, we employ a distant observer approximation, and in the above equation we take the LOS direction to be along the z -axis direction.

In this paper, we consider the cross-correlation between the IA shear of galaxy clusters and the galaxy density field. For the latter, we will use the spectroscopic sample of galaxies in the measurement. We can define the coordinate-independent cross-correlation function as

$$\xi_{g+}(\mathbf{r}) \equiv \langle \gamma_+(\mathbf{x}; \mathbf{x}') \delta_g(\mathbf{x}') \rangle, \quad (2)$$

with γ_+ being defined as

$$\gamma_+(\mathbf{x}; \mathbf{x}') \equiv \Re \left[(\gamma_1(\mathbf{x}) + i\gamma_2(\mathbf{x})) e^{-2i\phi_r} \right]. \quad (3)$$

Here \Re denotes a notation to take the real part of the cluster shear, $\mathbf{r} \equiv \mathbf{x} - \mathbf{x}'$, and ϕ_r is the angle measured from the first coordinate axis to the projected separation vector \mathbf{r}_p on the sky plane perpendicular to the LOS direction. Since we can measure only the projected shape of each cluster and the positions of clusters and galaxies are modulated by redshift-space distortion (RSD) (Kaiser 1987), the 3D cross-correlation function is generally given as a function of the 3D separation vector $\mathbf{r} = (r_{\parallel}, \mathbf{r}_p)$, where r_{\parallel} is the component parallel to the LOS direction and \mathbf{r}_p is the 2D separation vector perpendicular to the LOS.

Following the formulation in Kurita & Takada (2022) (also see Kurita & Takada 2023) and as derived in Appendix A, it is convenient to use the multipole moments of the cross-correlation function using the associated Legendre polynomials with $m = 2$, denoted as \mathcal{L}_ℓ^2 :

$$\xi_{g+}(r_p, r_{\parallel}) \equiv \sum_{\ell \geq 2} \xi_{g+}^{(\ell)}(r) \mathcal{L}_\ell^2(\mu_r), \quad (4)$$

where μ_r is the cosine angle between \mathbf{r} and the LOS direction and $\xi_{g+}^{(\ell)}$ is the ℓ -th order multipole moment. Note that the multipole index ℓ starts from 2 ($\ell = 2, 3, \dots$) and $\mathcal{L}_2^2(x) = 3(1 - x^2)$, $\mathcal{L}_4^2(x) = 15(1 - x^2)(7x^2 - 1)/2$, and so forth. The multipole moments $\xi_{g+}^{(\ell)}$ can also be expressed in terms of the cross-power spectrum using

$$\xi_{g+}^{(\ell)}(r) = i^\ell \int \frac{k^2 dk}{(2\pi)^2} P_{gE}^{(\ell)}(k) j_\ell(kr), \quad (5)$$

where $P_{gE}^{(\ell)}(k)$ is the corresponding multipole moments of the IA cross-power spectrum $P_{gE}(\mathbf{k})$.

Assuming the linear alignment model (equation 1) and the linear Kaiser RSD, the cross-power spectrum is given as

$$P_{gE}(\mathbf{k}, z) = b_g b_K \frac{(1 - \mu_{\mathbf{k}}^2)}{2} (1 + \beta \mu_{\mathbf{k}}^2) P_{\text{mm}}^{\text{NL}}(k, z), \quad (6)$$

where b_K is the linear shape bias parameter (Schmidt, Pajer & Zaldarriaga 2014; Akitsu, Li & Okumura 2021; Kurita et al. 2021), b_g is the linear bias parameter of the density sample, $\beta \equiv f(z)/b_g$, f is the logarithmic of linear growth rate, and $\mu_{\mathbf{k}}$ is the cosine angle between \mathbf{k} and the LOS direction. In Λ CDM cosmology/Universe, for a wide range of redshifts, $f(z) \sim \Omega_m(z)^{0.55}$. In the above equation, we used the non-linear matter power spectrum, $P_{\text{mm}}^{\text{NL}}$, including the effect of non-linear structure formation, which is the so-called non-linear alignment model (NLA) (Bridle & King 2007). Also note that we assumed the linear Kaiser RSD factor $(1 + \beta \mu_{\mathbf{k}}^2)$, but we will below consider the projected correlation function to minimize the RSD contribution. The shape bias parameter b_K is related to the IA amplitude parameter A_{IA} that is often used in the literature as

$$b_K = -2A_{\text{IA}} C_1 \rho_{\text{crit}} \frac{\Omega_m}{D(z)}, \quad (7)$$

where $D(z)$ is the linear growth factor and we take $C_1 \rho_{\text{crit}} = 0.0134$ following the convention (Joachimi et al. 2011). Throughout this paper we focus on A_{IA} to discuss the IA amplitude of redMaPPer clusters.

Using equation (6), the multipole moments of the cross-correlation function can be found, as derived in Appendix A, as

$$\begin{aligned} \xi_{g+}^{(2)}(r) &= \frac{b_g b_K}{6} \left(1 + \frac{\beta}{7} \right) \xi_{\text{mm}}^{(2)}(r), \\ \xi_{g+}^{(4)}(r) &= \frac{b_g b_K}{105} \beta \xi_{\text{mm}}^{(4)}(r), \end{aligned} \quad (8)$$

and zero otherwise. The multipole moments of the matter two-point correlation function is defined similarly to equation (5) using $P_{\text{mm}}^{\text{NL}}$. When there is no RSD effect, only the lowest order moment ($\ell = 2$)

carries all the IA cross-correlation information, which can be realized by the use of the associated Legendre polynomials (Kurita & Takada 2022).

In this paper we consider the projected IA cross-correlation function defined as

$$w_{g+}(r_p) = 2 \int dz W(z) \int_0^{\Pi_{\max}} dr_{\parallel} \xi_{g+}(r_{\parallel}, r_p; z). \quad (9)$$

We adopt $\Pi_{\max} = 100 h^{-1} \text{Mpc}$ as our fiducial choice.

To estimate the linear bias parameter of the density sample, b_g , we model the galaxy clustering signal using

$$w_{gg}(r_p) = 2 \int dz W(z) f_{\text{corr}}(r_p, z) \int_0^{\Pi_{\max}} dr_{\parallel} b_g^2 \xi_{\text{mm}}^{\text{NL}} \left(\sqrt{r_p^2 + r_{\parallel}^2}, z \right), \quad (10)$$

where $f_{\text{corr}}(r_p, z)$ is Kaiser correction factor given by (van den Bosch et al. 2013)

$$f_{\text{corr}}(r_p, z) = \frac{\int_0^{\Pi_{\max}} \xi_{\text{gg}}^{\text{lin}}(r_p, r_{\parallel}, z) dr_{\parallel}}{\int_0^{\Pi_{\max}} \xi_{\text{gg}}^{\text{lin}}(\sqrt{r_p^2 + r_{\parallel}^2}, z) dr_{\parallel}}. \quad (11)$$

$\xi_{\text{gg}}^{\text{lin}}(r_p, r_{\parallel}, z)$ and $\xi_{\text{gg}}^{\text{lin}}(r \equiv \sqrt{r_p^2 + r_{\parallel}^2}, z)$ here are the linear two-point galaxy correlation function in redshift space and real space, respectively, where $\xi_{\text{gg}}^{\text{lin}}(r, z) = b_g^2 \xi_{\text{mm}}^{\text{lin}}(r, z)$ and the linear galaxy correlation function in redshift space is

$$\xi_{\text{gg}}^{\text{lin}}(r_p, r_{\parallel}, z) = \sum_{l=0}^2 \xi_{2l}(s, z) \mathcal{P}_{2l}(\mu). \quad (12)$$

$s = \sqrt{r_p^2 + r_{\parallel}^2}$ is the real space separation, $\mu = r_{\parallel}/s$, and $\mathcal{P}_{2l}(x)$ is the l -th Legendre polynomial. ξ_0, ξ_2 , and ξ_4 are given by

$$\xi_0(r, z) = \left(1 + \frac{2}{3}\beta + \frac{1}{5}\beta^2 \right) \xi_{\text{gg}}^{\text{lin}}(r, z), \quad (13)$$

$$\xi_2(r, z) = \left(\frac{4}{3}\beta + \frac{4}{7}\beta^2 \right) \left[\xi_{\text{gg}}^{\text{lin}}(r, z) - 3J_3(r, z) \right], \quad (14)$$

$$\xi_4(r, z) = \frac{8}{35}\beta^2 \left[\xi_{\text{gg}}^{\text{lin}}(r, z) + \frac{15}{2}J_3(r, z) - \frac{35}{2}J_5(r, z) \right], \quad (15)$$

where

$$J_n(r, z) = \frac{1}{r^n} \int_0^r \xi_{\text{gg}}^{\text{lin}}(y, z) y^{n-1} dy. \quad (16)$$

To compute the model predictions of the projected IA cross-correlation (equation 9), we assume the Λ CDM cosmology with $\Omega_{\text{DM}} = 0.236$, $\Omega_{\text{b}} = 0.046$, $\Omega_{\Lambda} = 0.718$, $n_s = 0.9646$, $\sigma_8 = 0.817$, and $h = 0.7$ (WMAP9 cosmology, Hinshaw et al. 2013). For the non-linear matter power spectrum, we employ `Halofit`⁷ for the Λ CDM model (Takahashi et al. 2012). We vary the linear bias parameters b_g and b_K (equivalently A_{IA}) and estimate the best-fitting values by comparing the model predictions with the measurements for the Λ CDM model.

3 DATA

3.1 BOSS DR12 LOWZ galaxies

We use SDSS-III BOSS DR12 LOWZ galaxies with spectroscopic redshifts in the range of $0.1 \leq z \leq 0.33$ as a biased tracer of the

matter field. This is due to their significant overlap with redMaPPer clusters. The LOWZ sample consists of LRGs at $z < 0.4$, selected from the SDSS DR8 imaging data and observed spectroscopically in the BOSS survey. The sample is roughly volume-limited in the redshift range $0.16 < z < 0.36$ and has a mean number density of $\sim 3 \times 10^{-4} h^3 \text{Mpc}^{-3}$. We utilize the large-scale structure catalogues⁸ for BOSS (Anderson et al. 2012; Rykoff et al. 2016). Table 1 provides an overview of the properties of the density sample. The final density sample contains 239 904 galaxies. We apply a weighting scheme to sample, using $w = w_{\text{FKP}} \times w_{\text{tot}}$, where $w_{\text{tot}} = w_{\text{sys}} \times (w_{\text{cp}} + w_{\text{noz}} - 1)$ for density data and $w = w_{\text{FKP}}$ for density random.

3.2 redMaPPer cluster

We use galaxy clusters identified with redMaPPer algorithm (Rozo & Rykoff 2014; Rykoff et al. 2014) on SDSS DR8 photometry data (Aihara et al. 2011), over an area of about $10\,000 \text{deg}^2$. The redMaPPer algorithm finds optical clusters via identifying overdensity of red sequence galaxies. We use the publicly available version, v6.3. For each cluster, the algorithm provides potential brightest central galaxy (BCG) candidates, cluster richness λ which is the sum-up of p_{mem} over all candidates members, photometric redshift z_{λ} , and spectroscopic redshift z_{spec} if available. p_{mem} gives the membership probability of each galaxy belonging to a cluster in the redMaPPer catalogue. We choose the galaxies with the highest p_{cen} as BCGs. In this paper we use galaxy clusters that have available z_{spec} , and select clusters with $20 \leq \lambda \leq 200$ and $0.1 \leq z_{\text{spec}} \leq 0.33$. We further divide the sample into subsamples with $20 \leq \lambda < 30$, $30 \leq \lambda < 40$, $40 \leq \lambda < 55$, $55 \leq \lambda < 200$, in order to study the richness dependence of A_{IA} . The statistical properties of the redMaPPer clusters are summarized in Table 1.

We use the public random catalogue of redMaPPer cluster, which includes cluster positions, redshift, richness λ , and weight. The weighted z and λ distributions are the same as in the data. We apply the same z and λ cuts in the random catalogue for each cluster sample.

3.2.1 Cluster shape characterization – BCG versus member galaxy distribution

We quantify the shape of each redMaPPer cluster by two ways: the shape of BCGs, and the distribution of the member galaxies relative to BCGs. The BCG shape can be obtained by cross-matching with SDSS DR8 shear catalogue (Reyes et al. 2012). 4325 clusters have BCG shape measurement, out of 6345 selected clusters with $20 \leq \lambda \leq 200$.

Alternatively, we follow the method in van Uitert & Joachimi (2017) to quantify the cluster shape using member galaxy positions with respect to the BCG. Using all cluster members with $p_{\text{mem}} > 0.2$, the second moments of the projected shape are given as

$$I_{ij} = \frac{\sum_k (\theta_{i,k} - \theta_i^{\text{BCG}})(\theta_{j,k} - \theta_j^{\text{BCG}}) p_{\text{mem},k}}{\sum_k p_{\text{mem},k}}, \quad (17)$$

where $i, j \in 1, 2$.

The ellipticity components are then defined as

$$\epsilon_1 = \frac{I_{11} - I_{22}}{I_{11} + I_{22}}, \quad \epsilon_2 = \frac{2I_{12}}{I_{11} + I_{22}}. \quad (18)$$

The ‘shear’ of cluster shape is estimated as $\gamma_{1,2} = \epsilon_{1,2}/(2\mathcal{R})$, where $\mathcal{R} \equiv 1 - \langle \epsilon_i^2 \rangle$ is the shear responsivity (Bernstein & Jarvis 2002).

⁷<https://pyhalofit.readthedocs.io/>

⁸<https://data.sdss.org/sas/dr12/boss/lss/>

Table 1. Summary of the sample properties. For the samples in mock observe catalogue, we select clusters based on observed richness λ_{obs} with γ_{obs} ; while for mock true, we use true richness λ_{true} with γ_{true} . N_g and N_{clus} are number of galaxies and clusters in the samples separately. $\langle \lambda \rangle$ is the mean richness parameter of the sample. $\epsilon_{\text{RMS}}^2 = \langle \epsilon_i^2 \rangle$ is the RMS ellipticity. b_g and b_{clus} are bias of the samples. The error bars of b_{clus} in the mock indicate the 1σ scatter among the 19 mock realizations. A_{IA} is the IA strength parameter obtained from fitting with NLA model. The error bars of A_{IA} indicate the 1σ scatter among the 19 mock realizations.

Observation data set	N_g	$\langle \lambda \rangle$	ϵ_{RMS}	b_g	A_{IA}
LOWZ galaxy	239 904	–	–	1.73 ± 0.05	–
cluster w/ BCG shape ($\lambda \geq 20$)	4325	33.1	0.20	3.93 ± 0.29	11.5 ± 3.9
cluster ($\lambda \geq 20$)	6345	33.0	0.21	4.69 ± 0.25	17.4 ± 3.7
cluster ($20 \leq \lambda < 30$)	3593	24.2	0.22	4.12 ± 0.36	17.8 ± 5.0
cluster ($30 \leq \lambda < 40$)	1492	34.3	0.20	4.73 ± 0.64	16.9 ± 6.7
cluster ($40 \leq \lambda < 55$)	786	46.4	0.19	5.53 ± 1.18	10.9 ± 7.9
cluster ($55 \leq \lambda < 200$)	474	73.0	0.18	6.46 ± 1.46	24.5 ± 12.1
Mock observe	$\langle N_{\text{clus}} \rangle$	$\langle \lambda_{\text{obs}} \rangle$	RMS ϵ_{obs}	b_{clus}	A_{IA}
haloes ($M_h > 10^{12} h^{-1} M_{\odot}$)	–	–	–	1.17 ± 0.02	–
cluster ($20 \leq \lambda < 200$)	11 447	32.3	0.23	$3.79_{-0.06}^{+0.08}$	$14.0_{-0.9}^{+0.6}$
cluster ($20 \leq \lambda < 30$)	7002	24.0	0.24	$3.35_{-0.13}^{+0.07}$	$12.7_{-0.8}^{+0.6}$
cluster ($30 \leq \lambda < 40$)	2328	34.2	0.22	$4.04_{-0.32}^{+0.13}$	$14.7_{-1.8}^{+0.8}$
cluster ($40 \leq \lambda < 55$)	1278	46.1	0.20	$4.45_{-0.43}^{+0.36}$	$16.7_{-2.3}^{+2.4}$
cluster ($55 \leq \lambda < 200$)	839	75.3	0.19	$5.56_{-0.62}^{+0.45}$	$19.6_{-1.4}^{+1.7}$
Mock true	$\langle N_{\text{clus}} \rangle$	$\langle \lambda_{\text{true}} \rangle$	RMS ϵ_{true}	b_{clus}	A_{IA}
cluster ($20 \leq \lambda < 200$)	12 848	33.7	0.32	$3.28_{-0.09}^{+0.10}$	$37.3_{-0.3}^{+0.5}$
cluster ($20 \leq \lambda < 30$)	7329	23.6	0.34	$2.84_{-0.14}^{+0.15}$	$34.2_{-0.6}^{+1.6}$
cluster ($30 \leq \lambda < 40$)	2673	33.8	0.31	$3.42_{-0.31}^{+0.19}$	$37.6_{-2.7}^{+1.3}$
cluster ($40 \leq \lambda < 55$)	1590	45.8	0.30	$3.68_{-0.22}^{+0.37}$	$41.6_{-1.6}^{+2.2}$
cluster ($55 \leq \lambda < 200$)	1255	77.9	0.29	$4.86_{-0.28}^{+0.27}$	$47.5_{-4.1}^{+1.8}$

3.3 Correlation function estimator

For the BOSS LOWZ sample and the specp- z matched redMaPPer cluster, we measure the autocorrelation function of LOWZ galaxies, $\xi_{\text{gg}}(\mathbf{r})$, and the projected IA cross-correlation function between the LOWZ galaxy and the redMaPPer cluster shapes, $\xi_{g+}(\mathbf{r})$.

We use a generalized Landy–Szalay estimator (Landy & Szalay 1993) for estimating the correlation functions:

$$\hat{\xi}_{g+} = \frac{S_+ D - S_+ R_D}{R_S R_D}, \quad (19)$$

$$\hat{\xi}_{gg} = \frac{DD - 2DR + RR}{RR}, \quad (20)$$

where S_+ is the shape field for the cluster sample, D is the density field for the LOWZ galaxy sample, and R_S and R_D are random points corresponding to shape sample and density sample, respectively. S_+ is the $+$ -component of cluster shear with respect to the vector $\mathbf{r} \equiv \mathbf{x} - \mathbf{x}'$ connecting the cluster position and the LOWZ galaxy or the density random point (see equation 3).

For the IA cross-correlation, we consider the projected correlation function:

$$\hat{w}_{g+}(r_p) = \int_{-\Pi_{\text{max}}}^{\Pi_{\text{max}}} d\Pi \hat{\xi}_{g+}(r_{\parallel}, r_p). \quad (21)$$

We compare the measured w_{g+} with the theory prediction (equation 9).

3.4 redMaPPer cluster mock

To study the impact of projection effects on IA of galaxy clusters, we use the cluster mock catalogue constructed in Sunayama & More

(2019) (see also Sunayama et al. 2020 and Sunayama 2023). Here we briefly summarize the mock construction procedures, and refer the readers to Sunayama & More (2019) for more detailed information.

To construct the cluster mock, N -body simulations from Nishimichi et al. (2019) are used, which were performed with 2048^3 particles in a comoving cubic box with side length of $1 h^{-1}$ Gpc. The simulations adopt the *Planck* Cosmology (Planck Collaboration XIII 2016). The particle mass is $1.02 \times 10^{10} h^{-1} M_{\odot}$. Haloes are identified using Rockstar halo finder (Behroozi, Wechsler & Wu 2013), and M_{200m} is adopted for halo mass, which is the total mass within R_{200m} . R_{200m} is the radius within which the mean density is 200 times the mean mass density $\bar{\rho}_m$. For our purpose, we use the simulation snapshot and halo catalogues at $z = 0.25$, which is the mean redshift of the redMaPPer clusters. We have 19 realizations of N -body simulation and cluster mock.

Mock galaxies are populated into haloes with mass $M_{200m} > 10^{12} h^{-1} M_{\odot}$ using halo occupation distribution (HOD) prescription (Zheng et al. 2005). The HOD parameters are chosen to match with the abundance and lensing measurements of the redMaPPer clusters. Instead of distributing the satellite galaxies using Navarro–Frenk–White profile (Navarro, Frenk & White 1997), the satellites are populated using the positions of randomly selected member particles in each halo. As a result, the satellites distribution within the halo traces the non-spherical halo shape, which is also used as one of the validation tests in Appendix B.

The photometric redshift uncertainty, which is the main source of the projection effects, is modelled assuming a specific projection length, d_{proj} . In this work, we use the mock with $d_{\text{proj}} = 60 h^{-1}$ Mpc. The cluster finder which mimics the redMaPPer algorithm (Roza & Rykoff 2014; Rykoff et al. 2014) is then run on the red-sequence

mock galaxies, producing the mock cluster catalogue that includes the true richness λ_{true} , the observed richness λ_{obs} , and the membership probability p_{mem} . The galaxy in the most massive halo in each identified cluster is considered as the central galaxy of the cluster. The optical radial cut that scales with the richness, $R_c(\lambda) = R_0(100/\lambda)^\beta$, is applied the same way as in observation when running the redMaPPer algorithm in mock, where $R_0 = 1.0 h^{-1} \text{ Mpc}$ and $\beta = 0.2$.

Similar as in observation, we divide the mock cluster sample into subsamples with various richness bins, using both λ_{obs} and λ_{true} . We use haloes with $M_{200m} > 10^{12} h^{-1} M_\odot$ as density tracers, δ_h , of the matter field, where $\delta_h \equiv \frac{n_h(\mathbf{x}) - \bar{n}_h}{\bar{n}_h}$. The properties of the selected cluster samples are shown in Table 1. The cluster bias increases with the richness, which is consistent with the fact that halo/cluster mass increases with richness. Sunayama et al. (2020) presented the halo mass distribution of the mock clusters in different richness bins (divided by both λ_{obs} and λ_{true}), showing that mass distributions for the ‘**mock observe**’ sample is more extended than the ‘**mock true**’ sample because of the projection effects, also the peak mass shifts towards higher masses from finite aperture effects in higher richness bins. This explains the higher cluster bias for ‘**mock observe**’ sample shown in Table 1.

3.4.1 Cluster shape characterization

For each galaxy cluster in the mock, we calculate the observed cluster shape γ_{obs} using the redMaPPer member galaxies with $p_{\text{mem}} > 0.2$, using equation (17). Unlike observation, mock cluster catalogues provide the true positions of the satellite galaxies as well as the dark matter particles. So, we can calculate the intrinsic cluster shear γ_{true} using satellite galaxy positions and γ_{DM} using DM particles distributions (see Appendix B for details of the calculation). The IA signal measured from γ_{true} agrees with that from γ_{DM} very well (see Appendix B). So in the following text, we take mock clusters selected using λ_{true} and shape calculated using γ_{true} as the ‘**mock true**’ sample, while mock cluster selected using λ_{obs} and γ_{obs} as the ‘**mock observe**’ sample.

We use TreeCorr (Jarvis, Bernstein & Jain 2004) to compute the correlation functions. We measured the signal as a function of transverse comoving separation in 25 logarithmic bins between 0.1 and 200 $h^{-1} \text{ Mpc}$. We take $\Pi_{\text{max}} = 100 h^{-1} \text{ Mpc}$ and 20 linear bins for $r_{\parallel} \in [-100, 100] h^{-1} \text{ Mpc}$. To estimate the covariance matrix, we divide the redMaPPer Cluster sample into 50 jackknife regions of approximately equal area on the sky, and compute the cross-correlation function by excluding one region each time (Norberg et al. 2009). For the mock cluster sample, we divide the simulation box into 64 sub-boxes of equal volume for jackknife covariance matrix estimation.

We restricted the analysis to mildly non-linear scales of $r_p > 6 h^{-1} \text{ Mpc}$. The size of the jackknife patch is 14 deg, which roughly corresponds to 70 $h^{-1} \text{ Mpc}$ at $z = 0.1$. So we take 70 $h^{-1} \text{ Mpc}$ as the maximum scale in the fitting.

4 RESULTS

4.1 IA of redMaPPer clusters in SDSS

The measured cross-correlation functions of the galaxy density field and the cluster shape field are shown in Fig. 1. Here we used the cluster shapes measured using positions of the member galaxies relative to the BCG in each cluster. We obtain a clear detection of IA signal in all richness bins, meaning that cluster shapes have correlations with the surrounding large-scale structures.

The IA amplitude, A_{IA} , is obtained by fitting NLA model to the measurement, as introduced in Section 2. However, A_{IA} is degenerate with bias parameter b_g of the galaxy density sample. We obtain $b_g = 1.73 \pm 0.05$ by measuring and fitting the projected clustering signal of LOWZ galaxies to the model (equation 10), as shown in Fig. 2. We have good fits of the model prediction, with reduced χ^2 value of 1.02. Our result for the LOWZ galaxy bias is consistent with the previous measurement, $b_g = 1.77 \pm 0.04$, in Singh, Mandelbaum & More (2015). We ascribe the slight difference to the different redshift range, where they used $0.16 < z < 0.36$ compared to our range, $0.10 \leq z \leq 0.33$.

The IA amplitude of each subsample can be found in Table 1. The NLA model gives a good fit to the measured w_{g+} in the fitting range of $6 h^{-1} \text{ Mpc} < r_p < 70 h^{-1} \text{ Mpc}$ for each cluster sample. However, at small scales, the model predictions are much lower than the measured signal. The IA amplitude, A_{IA} , does not show a clear dependence on cluster richness. This contradicts with the results found from the shapes of haloes in simulations (Kurita et al. 2021); they found that A_{IA} increases with halo mass. We found this is mainly caused by the projection effects, as we will discuss in Section 4.3 in detail.

4.1.1 Tests for systematics

In Fig. 3 we study potential systematic effects in our IA measurements. The upper panel shows the measured correlation function between the cross-component of the cluster shape, γ_{\times} , and the galaxy density field, $w_{g \times}$, for the sample with $20 \leq \lambda < 200$. This cross-correlation should be vanishing due to parity symmetry if the measurements is not affected by an unknown systematic effect. We also show the IA cross-correlation function, w_{g+} , measured by integrating the original 3D IA correlation function only over the large LOS separation, $150 h^{-1} \text{ Mpc} < |\Pi| < 500 h^{-1} \text{ Mpc}$. This cross-correlation is expected to have a very small signal, if the redshift of clusters is accurate or if there is no significant contamination of fake clusters due to the projection effect. The measured w_{g+} for the large $|\Pi|$ separation shows a very small signal. Hence we conclude that our measurements are not affected by the \times -component or the fake clusters.

There are other potential systematic effects that affect our IA measurements. These include photometric redshift errors, errors in cluster shape estimation arising due to a limited number of member galaxies, miscentring effect, contamination of merging clusters, and incompleteness of cluster sample or selection function. van Uitert & Joachimi (2017) presented the tests of above systematic effects for the redMaPPer cluster sample, and showed that the most significant systematic effect arises from photo- z errors for the cluster sample. Since we use only the clusters that have spectroscopic redshifts, we conclude that our IA measurements are not affected by the photo- z errors.

However, we show next that the projection effect due to large-scale structure surrounding the redMaPPer clusters causes a systematic contamination to the IA measurements.

4.2 IA of clusters in mock – impact of projection effect

In Fig. 4 we study the impact of the projection effect on the IA correlation functions using the mock catalogue of redMaPPer clusters. To do this, we compare the IA correlation functions for clusters using the true or ‘observed’ richness (λ_{true} or λ_{obs}) and/or the true or ‘observed’ shape estimates (γ_{true} or γ_{obs}), where the observed quantities are affected by the projection effect. The figure shows that the IA correlation function using the observed quantities (λ_{obs} and γ_{obs}) displays

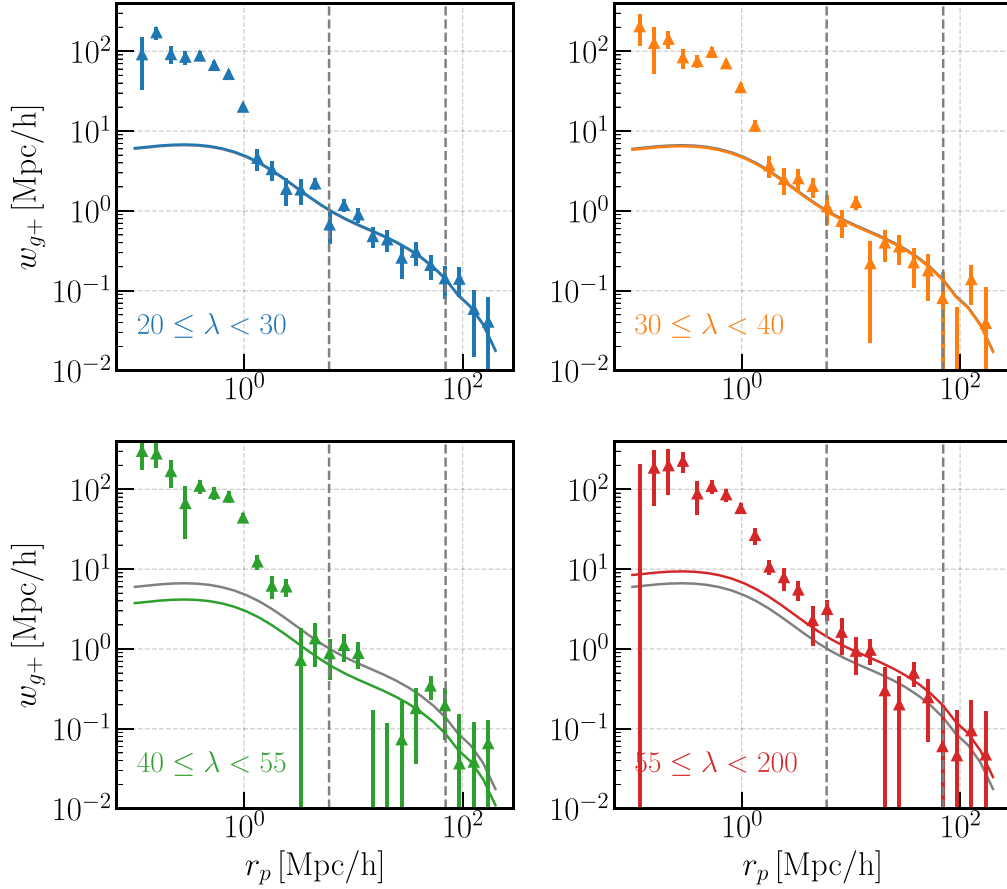


Figure 1. The LOWZ galaxy–cluster shape correlation, w_{g+} , of clusters in the redshift range of $0.1 \leq z \leq 0.33$. The different panels show the result for various richness bins. The dots are measurement from data, and the coloured solid lines are the fitting using NLA in the range of $6 h^{-1} \text{ Mpc} < r_p < 70 h^{-1} \text{ Mpc}$. The grey solid line shows the fitting result for the cluster sample with $20 \leq \lambda < 200$, just to guide the eyes.

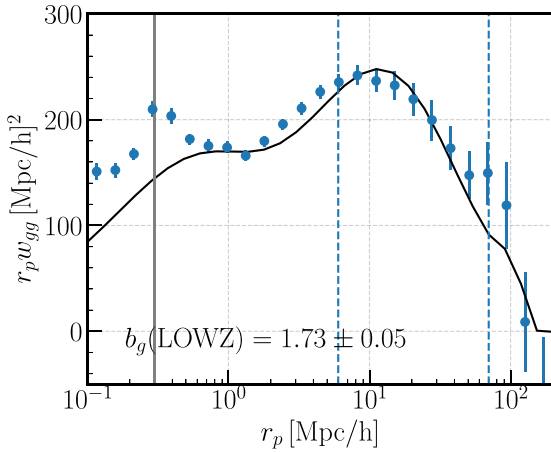


Figure 2. The galaxy–galaxy correlation, w_{gg} , of the LOWZ sample in the redshift range of $0.1 \leq z \leq 0.33$. The blue dots are measurement from data, and the black solid line is the fitting using linear model with non-linear matter power spectrum in the range of $6 h^{-1} \text{ Mpc} < r_p < 70 h^{-1} \text{ Mpc}$. The grey solid line shows the SDSS fibre collision scale at $z = 0.33$.

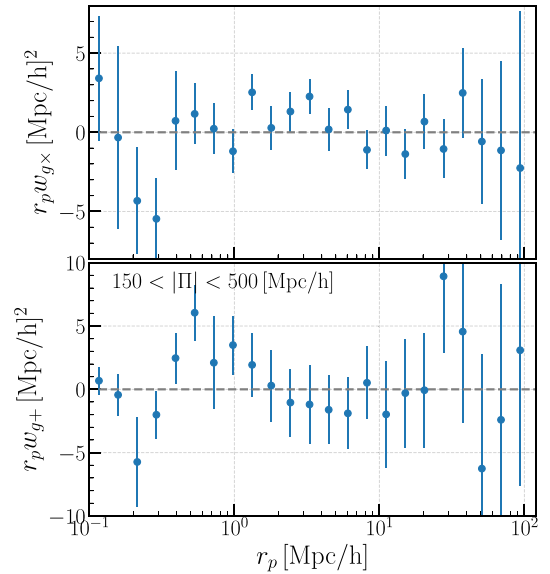


Figure 3. Tests of systematic effects in the IA measurement of galaxy clusters with $20 \leq \lambda < 200$. *Upper panel:* cross-correlation between LOWZ galaxies and redMaPPer cluster shape γ_{\times} , the signal is consistent with 0. *Lower panel:* measurement of w_{g+} within $150 < |\Pi| < 500 h^{-1} \text{ Mpc}$, the signal is also consistent with null signal.

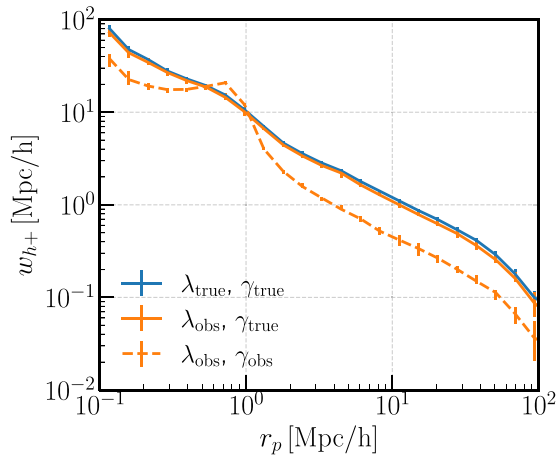


Figure 4. The IA correlation functions measured for galaxy clusters in the mock simulations, selected using $20 \leq \lambda_{\text{obs}} < 200$ (blue) and $20 \leq \lambda_{\text{true}} < 200$ (orange), respectively. The solid lines show the measurements using γ_{true} , i.e. satellites distributions within dark matter haloes, while the dashed line shows the measurement using γ_{obs} , i.e. member galaxies identified by redMaPPer algorithm. The lines here show the median values among 19 realizations, and the error bars are the 1σ dispersion.

about factor of 2 smaller amplitudes than that for non-contaminated clusters (λ_{true} and γ_{true}). The solid orange curve shows the result when using the clusters for λ_{obs} and γ_{true} , which show almost similar amplitudes to that for the non-contaminated clusters (λ_{true} and γ_{true}). The comparison tells that the smaller amplitude for the case of (λ_{obs} , γ_{obs}) is caused mainly by the projection effect on the shape measurement (γ_{obs} against γ_{true}). The A_{IA} values estimated from w_{h+} for the different samples are given in Table 1. Fig. 4 only shows the result for the cluster sample with $20 \leq \lambda < 200$, the measurement and fitting results for other richness bins are shown in Appendix C.

When comparing the solid and dashed lines in Fig. 4, we notice the existence of a bump in w_{h+} around $r_p \sim 1 h^{-1}$ Mpc for the case with projection effects. Here $1 h^{-1}$ Mpc roughly corresponds to the aperture size used in the redMaPPer cluster finder (Rykoff et al. 2014). We will show later that this specific imprint of projection effects is likely caused by the non-member interlopers, which are however identified as cluster members by the redMaPPer method, and the real member galaxies that are missed by the cluster finder.

4.2.1 f_{true} and f_{miss}

As we have found, the projection effect impacts the shape estimation of clusters. There are two effects: one is caused by including interlopers (non-member galaxies) in the cluster members, and the other is caused by missing real member galaxies, when estimating the cluster shape. To study how these two effects cause a contamination to the IA correlation function, we define the following quantities:

(i) $f_{\text{true}} = \frac{\sum_{d_i \leq R_c} p_{\text{mem},i}^{\text{true}}}{\lambda_{\text{obs}}}$, which is the true member fraction of identified members in each cluster. This quantity is the same as that used in Sunayama et al. (2020),

(ii) $f_{\text{miss}} = 1 - n_{\text{true, mem}}(< R_c) / \lambda_{\text{true}}$, which is the fraction of true members missed in the membership identification in each cluster.

Here $p_{\text{mem},i}^{\text{true}}$ is the membership probability of the i -th true member galaxy identified by the redMaPPer finder, R_c is the cluster radius used in the redMaPPer finder, and $n_{\text{true, mem}}$ is the number of true

member galaxies among all redMaPPer member galaxies. Note $0 < f_{\text{true}} \leq 1$ by definition, and $f_{\text{true}} = 1$ means that the redMaPPer finder-identified member galaxies are true member galaxies that belong to the cluster, and no interlopers contaminate the true membership (however, all the true members are not necessarily identified). On the other hand, a low f_{true} indicates a higher contamination fraction of interlopers. f_{miss} informs how many true member galaxies are not identified as member galaxies by the cluster finder.

In Fig. 5, we show the ratio of $w_{h+}(\gamma_{\text{obs}})$ versus $w_{h+}(\gamma_{\text{true}})$ for samples with low f_{true} (f_{miss}) and high f_{true} (f_{miss}) separately. If the ratio between $w_{h+}(\gamma_{\text{obs}})$ and $w_{h+}(\gamma_{\text{true}})$ is close to 1 for a subsample, it means the measured cluster shape/IA are less affected by the projection effects. On the contrary, if the ratio deviates from unity more, it means the projection effect is making the measured shape/IA deviate from the underlying true signals. Fig. 5 shows that the impact on large-scale IA signal of projection effects is weaker for clusters with high f_{true} and low f_{miss} , compared to the clusters with low f_{true} and high f_{miss} . The amplitude of the bump at $r_p \sim 1 h^{-1}$ Mpc is significantly decreased for samples with higher f_{true} and higher f_{miss} . As shown in Fig. 4, the bump only appears when the projection effect is included in the mock, i.e. for $w_{h+}(\gamma_{\text{obs}})$.

4.2.2 Coupling between cluster IA and projection effects

Cluster IA and projection effects are coupled with each other. In Fig. 6, we compare the IA signal of low f_{true} (f_{miss}) and high f_{true} (f_{miss}) subsamples. The large-scale IA amplitude is higher when f_{miss} or f_{true} is higher, for both γ_{obs} and γ_{true} . The coupling between cluster IA and projection effects are illustrated by the cartoons shown in Fig. 7.

For clusters with their major axis (orientation) perpendicular to the LOS direction, the measured IA is higher, since their projected shapes appear more elliptical and we measured the cross-correlation between the projected shapes and the density field. These clusters also tend to have LSS structures, such as filaments, that are perpendicular to the LOS direction. The missed member galaxy fraction f_{miss} is higher, since the projected member galaxies distribution is more dispersed; and the contamination from interlopers is lower, since there are less galaxies outside the cluster along the LOS, thus f_{true} is higher. In contrast, for clusters with their major axis along the LOS direction, the measured IA is lower, and it is more likely to have LSS structures along the LOS; they are less likely to miss galaxy members (lower f_{miss}) since they are concentrated in the inner region; the contamination from interlopers along the LOS is higher (lower f_{true}). In both cases, the outer region of the cluster is affected more, since the member number density decreases with the distance from the cluster centre. This likely explains the existence of the bump at $r_p \sim 1 h^{-1}$ Mpc, which is also the typical cluster boundary. The above picture is supported by Fig. D1 in Appendix D, where we show that clusters with lower f_{true} and lower f_{miss} tend to have their major axis parallel with the LOS direction. In summary, the above picture explains the coupling between cluster IA and f_{miss} , f_{true} .

4.3 Dependence on cluster richness

The impact of the projection effects on cluster IA is independent of the cluster richness, as shown in Fig. 8. The ratios of $w_{h+}(\text{obs})$ with projection effects versus $w_{h+}(\text{true})$ without projection effects at scales of $6 h^{-1}$ Mpc $< r_p < 70 h^{-1}$ Mpc is roughly constant and does not depend on the richness of the clusters.

In Fig. 9, we plot the measured A_{IA} versus cluster mean richness for redMaPPer clusters in observation, and clusters in the mock

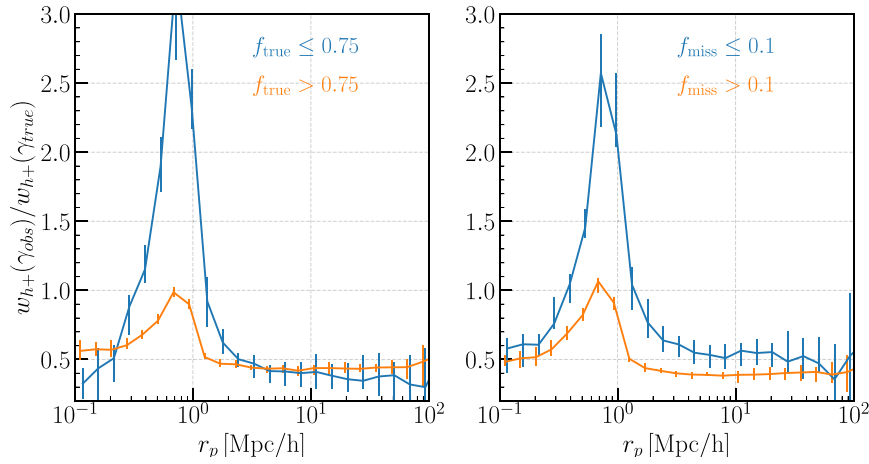


Figure 5. The IA correlation functions measured from the mock cluster catalogues. Shown is the ratio of the IA correlation function using the observed shape (γ_{obs}) to that of the true shape (γ_{true}), for a subsample of the mock clusters with $20 \leq \lambda_{\text{obs}} < 200$. *Left panel:* the ratio $w_{h+}(\gamma_{\text{obs}})/w_{h+}(\gamma_{\text{true}})$ for subsamples with $f_{\text{true}} \leq 0.75$ and $f_{\text{true}} > 0.75$, respectively, where f_{true} is the fraction of true members among the cluster members identified by the redMaPPer finder in each cluster. *Right:* the ratio for subsamples divided by $f_{\text{miss}} \leq 0.1$ and $f_{\text{miss}} > 0.1$, where f_{miss} is the fraction of true members missed by the finder in each cluster.

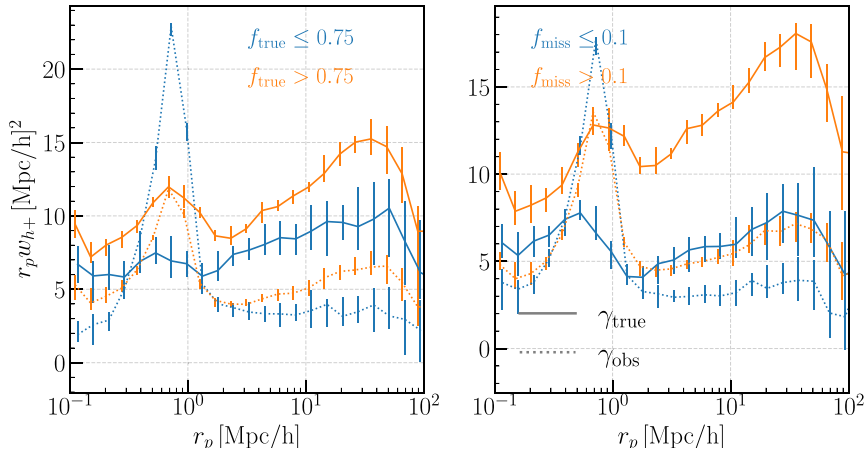


Figure 6. Similar to the previous figure, but we show the IA correlation functions, instead of the ratio. The solid lines are the IA correlation functions measured using γ_{true} , and the dotted lines are those measured using γ_{obs} .

with $w_{h+}(\text{true})$ (filled squares) and $w_{h+}(\text{obs})$ (open squares). The A_{IA} from observation agree with results using $w_{h+}(\text{obs})$ from mock pretty well, indicating that our mock construction and inclusion of the projection effects is quite reasonable. A weak increase of A_{IA} with respect to cluster richness can be seen for clusters free of projection effects. However, such dependence cannot be seen once projection effects are included. We further derived the A_{IA} –halo mass relation for galaxy clusters and compared it with the prediction from N -body simulation, which is shown in Appendix E.

5 DISCUSSION

5.1 Cluster IA using BCG shape versus member galaxy positions

The IA of BCGs are shown in Fig. 10. BCGs show a similar IA amplitude as the clusters that they lie in, indicating the good alignment of BCG orientations with respect to the member galaxies distribution of clusters. If we assume that the member galaxy distributions trace well the dark matter halo shapes, then the results in Fig. 10 could

hint a rather good alignment between BCG and dark matter haloes. However, previous studies of Okumura, Jing & Li (2009) showed that central LRGs are not perfectly aligned with the dark matter haloes, with a misalignment angle of ~ 35 deg. Recent work by Xu, Jing & Gao (2023) further showed that misalignment angles are likely to be mass-dependent. Nevertheless, the good alignment shown in Fig. 10 seems to be in contradiction with expectations from previous studies. We found this is mainly caused by the projection effects on the observed IA of redMaPPer clusters, which decreases the measured cluster IA signal using member galaxy positions. If the impact on cluster IA is uncorrected, the inferred misalignment angle between BCGs and clusters is smaller than it should have been.

6 SUMMARY

We measured the IA of galaxy clusters by cross-correlating the shapes of redMaPPer clusters with the LOWZ galaxies at $0.1 \leq z \leq 0.33$. We detected a positive IA signal, indicating that clusters point towards the density field. We also divide the samples into four richness samples, enabling us to study the dependence on cluster richness.

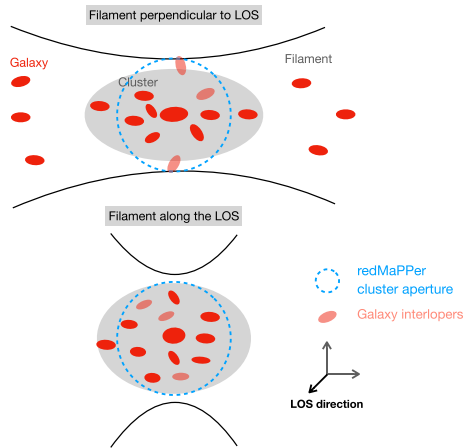


Figure 7. Cartoons illustrating the couplings between galaxy cluster IA and the projection effects, for clusters with their major axis perpendicular to the LOS direction (upper) and along the LOS direction (lower). For clusters with their major axis perpendicular to the LOS, the measured IA signal using projected cluster shape is stronger, the contamination fraction from interlopers is lower (i.e. higher f_{true}), and the missed galaxy member fraction is higher (i.e. higher f_{miss}); for clusters with their major axis parallel with the LOS direction, the measured IA signal is lower, the contamination from interlopers is more severe (i.e. lower f_{true}), and the missed member fraction is lower (i.e. lower f_{miss}).

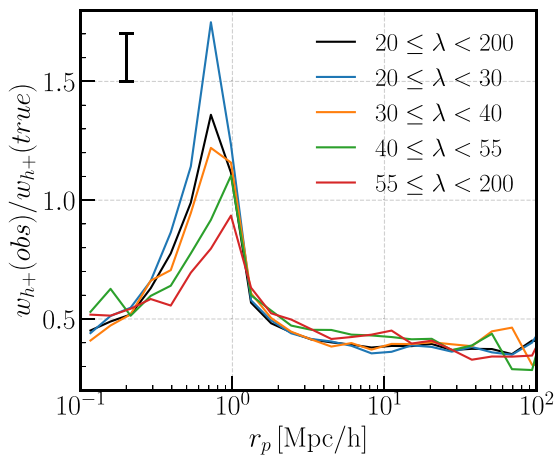


Figure 8. The ratio of the observed IA signal to the true IA signal of galaxy clusters in various richness bins in the mock. $w_{h+}(\text{obs})$ here is calculated using λ_{obs} and γ_{obs} , and $w_{h+}(\text{true})$ here is calculated using λ_{true} and γ_{true} . The typical 1σ scatter of the ratio among realizations is shown in the upper left corner of the plot.

We investigated the impact of projection effects on the measured IA of clusters using mock cluster catalogues. The inclusion of the projection effects decreases the measured IA signal by a factor of ~ 2.5 , which is almost independent of the cluster richness. The projection effects predominantly impact the measured cluster shapes, including interlopers that are not members of the clusters and missing true members. Consequently, projection effects lead to a smaller observed misalignment angle between BCG and clusters than the underlying one.

In our study, we discovered a correlation between cluster IA and projection effects. Clusters oriented parallel to the LOS are less likely to have undetected members and more likely to have interlopers, and

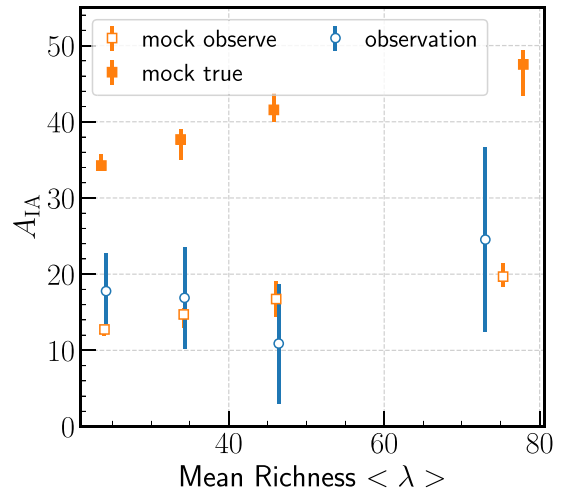


Figure 9. The A_{IA} versus richness λ relation for clusters in observation and mock catalogue. The blue open circles show the results from fitting the observed $w_{g+}(r_p)$ of redMaPPer clusters; the orange open squares are results from mock observe samples using λ_{obs} and γ_{obs} . The orange filled squares are results from mock true samples using λ_{true} and γ_{true} .

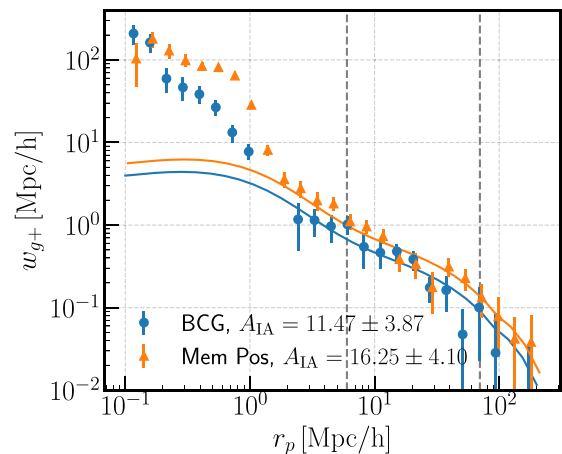


Figure 10. The LOWZ galaxy-BCG shape (blue) and LOWZ galaxy-cluster shape (orange) correlation, w_{g+} , of clusters with available BCG shapes in the redshift range of $0.1 \leq z \leq 0.33$. The blue and orange dots are measurement using BCG shapes and member galaxy positions, γ_{obs} , separately. The solid lines are the fitting results using NLA in the range of $6 h^{-1} \text{ Mpc} < r_p < 70 h^{-1} \text{ Mpc}$.

their projected shapes are less elliptical and exhibit weaker alignment signals. This can be attributed to their likely location within a filamentary structure along the LOS direction. Conversely, clusters oriented perpendicular to the LOS direction display a more elliptical projected shape and a stronger IA signal; they also tend to have a higher fraction of missed cluster members and a lower fraction of interlopers.

The measured IA strength, A_{IA} , in the cluster mock with projection effects agrees well with observation. The observed A_{IA} in both real data and mock observe clusters barely depends on cluster richness, while a weak dependence on richness does exist if we can correctly identify the true cluster members without any contamination.

Our work showed that IA measurements of galaxy clusters can be improved by identifying interlopers and by including the true member galaxies in the outer region, leading to a much higher signal-to-noise detection of cluster IA. High signal-to-noise detection of cluster IA

is crucial for applying IA as a novel cosmological probe. With more and more incoming spectroscopic data, we expect to suppress (or reduce) the impact of projection effects significantly. We will leave the efforts on removing projection effects for galaxy clusters to a future work.

ACKNOWLEDGEMENTS

We thank Teppei Okumura, Elisa Chisari, Ravi K. Sheth, Atsushi Taruya, and Khee-Gan Lee for enlightening discussion/comments on this work. This work was supported in part by World Premier International Research Center Initiative (WPI Initiative), MEXT, Japan, and JSPS KAKENHI Grant Numbers JP19H00677, JP20H05850, JP20H05855, JP20H05861, JP21H01081, and JP22K03634, and by Basic Research Grant (Super AI) of Institute for AI and Beyond of the University of Tokyo. The authors thank the Yukawa Institute for Theoretical Physics at Kyoto University. Discussions during the YITP workshop YITP-W-22-16 on New Frontiers in Cosmology with the Intrinsic Alignments of Galaxies were useful to complete this work. JS and TK also thank Lorentz Center and the organizers of the hol-IA workshop: a holistic approach to galaxy intrinsic alignments held from 2023 March 13 to 17.

DATA AVAILABILITY

The data underlying this article will be shared on reasonable request to the corresponding author.

REFERENCES

- Aihara H. et al., 2022, *PASJ*, 74, 247
 Aihara H. et al., 2011, *ApJS*, 193, 29
 Aihara H. et al., 2018, *PASJ*, 70, S4
 Akitsu K., Li Y., Okumura T., 2021, *J. Cosmol. Astropart. Phys.*, 2021, 041
 Anderson L. et al., 2012, *MNRAS*, 427, 3435
 Bailey V. P. et al., 2023, in *Society of Photo-Optical Instrumentation Engineers (SPIE) Conference Series*. p. 126800T ([arXiv:2309.08672](https://arxiv.org/abs/2309.08672))
 Behroozi P. S., Wechsler R. H., Wu H.-Y., 2013, *ApJ*, 762, 109
 Bernstein G. M., Jarvis M., 2002, *AJ*, 123, 583
 Bridle S., King L., 2007, *New J. Phys.*, 9, 444
 Catelan P., Kamionkowski M., Blandford R. D., 2001, *MNRAS*, 320, L7
 Cohn J. D., Evrard A. E., White M., Croton D., Ellingson E., 2007, *MNRAS*, 382, 1738
 Costanzi M. et al., 2019, *MNRAS*, 482, 490
 Dark Energy Survey Collaboration et al., 2016, *MNRAS*, 460, 1270
 Evans A. K. D., Bridle S., 2009, *ApJ*, 695, 1446
 Gonzalez E. J., Hoffmann K., Gaztañaga E., García Lambas D. R., Fosalba P., Crocce M., Castander F. J., Makler M., 2022, *MNRAS*, 517, 4827
 Hamilton A. J. S., 2015, *Astrophysics Source Code Library*, record ascl:1512.017
 Hinshaw G. et al., 2013, *ApJS*, 208, 19
 Hirata C. M., Seljak U., 2004, *Phys. Rev. D*, 70, 063526
 Jarvis M., Bernstein G., Jain B., 2004, *MNRAS*, 352, 338
 Joachimi B. et al., 2015, *Space Sci. Rev.*, 193, 1
 Joachimi B., Mandelbaum R., Abdalla F. B., Bridle S. L., 2011, *A&A*, 527, A26
 Kaiser N., 1987, *MNRAS*, 227, 1
 Kiessling A. et al., 2015, *Space Sci. Rev.*, 193, 67
 Kirk D. et al., 2015, *Space Sci. Rev.*, 193, 139
 Kuijken K. et al., 2015, *MNRAS*, 454, 3500
 Kurita T., Takada M., 2022, *Phys. Rev. D*, 105, 123501
 Kurita T., Takada M., 2023, *Phys. Rev. D*, 108, 083533
 Kurita T., Takada M., Nishimichi T., Takahashi R., Osato K., Kobayashi Y., 2021, *MNRAS*, 501, 833
 Landy S. D., Szalay A. S., 1993, *ApJ*, 412, 64

- Laureijs R. et al., 2011, preprint ([arXiv:1110.3193](https://arxiv.org/abs/1110.3193))
 LSST Science Collaboration et al., 2009, preprint ([arXiv:0912.0201](https://arxiv.org/abs/0912.0201))
 Mandelbaum R. et al., 2011, *MNRAS*, 410, 844
 Navarro J. F., Frenk C. S., White S. D. M., 1997, *ApJ*, 490, 493
 Nishimichi T. et al., 2019, *ApJ*, 884, 29
 Norberg P., Baugh C. M., Gaztañaga E., Croton D. J., 2009, *MNRAS*, 396, 19
 Oguri M., Takada M., Okabe N., Smith G. P., 2010, *MNRAS*, 405, 2215
 Okumura T., Jing Y. P., Li C., 2009, *ApJ*, 694, 214
 Osato K., Nishimichi T., Oguri M., Takada M., Okumura T., 2018, *MNRAS*, 477, 2141
 Park Y., Sunayama T., Takada M., Kobayashi Y., Miyatake H., More S., Nishimichi T., Sugiyama S., 2023, *MNRAS*, 518, 5171
 Planck Collaboration XIII, 2016, *A&A*, 594, A13
 Reyes R., Mandelbaum R., Gunn J. E., Nakajima R., Seljak U., Hirata C. M., 2012, *MNRAS*, 425, 2610
 Rozo E., Rykoff E. S., 2014, *ApJ*, 783, 80
 Rykoff E. S. et al., 2014, *ApJ*, 785, 104
 Rykoff E. S. et al., 2016, *ApJS*, 224, 1
 Schmidt F., Pajer E., Zaldarriaga M., 2014, *Phys. Rev. D*, 89, 083507
 Shin T.-h., Clampitt J., Jain B., Bernstein G., Neil A., Rozo E., Rykoff E., 2018, *MNRAS*, 475, 2421
 Simet M., McClintock T., Mandelbaum R., Rozo E., Rykoff E., Sheldon E., Wechsler R. H., 2017, *MNRAS*, 466, 3103
 Singh S., Mandelbaum R., More S., 2015, *MNRAS*, 450, 2195
 Smargon A., Mandelbaum R., Bahcall N., Niederste-Ostholt M., 2012, *MNRAS*, 423, 856
 Sunayama T. et al., 2020, *MNRAS*, 496, 4468
 Sunayama T., 2023, *MNRAS*, 521, 5064
 Sunayama T., More S., 2019, *MNRAS*, 490, 4945
 Takahashi R., Sato M., Nishimichi T., Taruya A., Oguri M., 2012, *ApJ*, 761, 152
 To C. et al., 2021, *Phys. Rev. Lett.*, 126, 141301
 Troxel M. A., Ishak M., 2015, *Phys. Rep.*, 558, 1
 van den Bosch F. C., More S., Cacciato M., Mo H., Yang X., 2013, *MNRAS*, 430, 725
 van Haarlem M. P., Frenk C. S., White S. D. M., 1997, *MNRAS*, 287, 817
 van Uitert E., Joachimi B., 2017, *MNRAS*, 468, 4502
 Weinberg D. H., Mortonson M. J., Eisenstein D. J., Hirata C., Riess A. G., Rozo E., 2013, *Phys. Rep.*, 530, 87
 Xu K., Jing Y. P., Gao H., 2023, *ApJ*, 954, 2
 Yao J., Shan H., Zhang P., Kneib J.-P., Jullo E., 2020, *ApJ*, 904, 135
 Zheng Z. et al., 2005, *ApJ*, 633, 791

APPENDIX A: NUMERICAL IMPLEMENTATION OF TWO-POINT CORRELATION FUNCTION

We here review the three-dimensional two-point statistics of shear. The goal of this section is to derive equation (8) in the main text.

A1 Two-point statistics

We assume the distant-observer (plane-parallel) approximation throughout this section. The shear of a cluster at a position \mathbf{x} is given by

$$\gamma(\mathbf{x}) = \gamma_1(\mathbf{x}) + i\gamma_2(\mathbf{x}). \quad (\text{A1})$$

This is a spin-2 quantity on the sky plane perpendicular to the LOS direction. To obtain the coordinate-independent shear for the two-point correlation function, we define the rotated shear with the radial and cross-components towards the other galaxy in a pair at a position \mathbf{x}' as

$$\gamma_{+, \times}(\mathbf{x}; \mathbf{x}') \equiv \gamma(\mathbf{x})e^{-2i\phi_{\mathbf{r}}}, \quad (\text{A2})$$

where $\mathbf{r} \equiv \mathbf{x} - \mathbf{x}'$ is the separation vector and $\phi_{\mathbf{r}}$ is the angle measured from the first coordinate axis to the projected separation

vector \mathbf{r}_p on the sky plane. The two-point cross-correlation function of the galaxy density and shear is defined by

$$\xi_{g\gamma}(\mathbf{r}) \equiv \langle \gamma_{+, \times}(\mathbf{x}; \mathbf{x}') \delta_g(\mathbf{x}') \rangle = \langle \gamma(\mathbf{x}) \delta_g(\mathbf{x}') \rangle e^{-2i\phi_r}, \quad (\text{A3})$$

where the radial and cross-components correspond to the real and imaginary parts, $\xi_{g+} = \Re \xi_{g\gamma}$, and $\xi_{g\times} = \Im \xi_{g\gamma}$, respectively.

In Fourier space, we start with the Fourier transform of equation (A1):

$$\gamma(\mathbf{k}) = \gamma_1(\mathbf{k}) + i\gamma_2(\mathbf{k}). \quad (\text{A4})$$

As in the case of configuration space, we define the coordinate-independent quantities in Fourier space, called *E/B* modes, with a similar rotation as

$$E(\mathbf{k}) + iB(\mathbf{k}) \equiv \gamma(\mathbf{k})e^{-2i\phi_{\mathbf{k}}}, \quad (\text{A5})$$

where $\phi_{\mathbf{k}}$ is the angle measured from the first coordinate axis to the wave vector on the sky plane. The cross-power spectrum of the galaxy density and shear is thus given by

$$(2\pi)^3 \delta_D(\mathbf{k} + \mathbf{k}') P_{g\gamma}(\mathbf{k}) \equiv \langle [E(\mathbf{k}) + iB(\mathbf{k})] \delta_g(\mathbf{k}') \rangle = \langle \gamma(\mathbf{k}) \delta_g(\mathbf{k}') \rangle e^{-2i\phi_{\mathbf{k}}}, \quad (\text{A6})$$

where the *E*- and *B*-mode spectra correspond to $P_{gE} = \Re P_{g\gamma}$ and $P_{gB} = \Im P_{g\gamma}$, respectively.

From equations (A3) and (A6), we obtain the relation between the correlation function and the power spectrum,

$$\xi_{g\gamma}(\mathbf{r}) = \int \frac{d\mathbf{k}}{(2\pi)^3} P_{g\gamma}(\mathbf{k}) e^{2i(\phi_{\mathbf{k}} - \phi_r)} e^{i\mathbf{k}\cdot\mathbf{r}}. \quad (\text{A7})$$

These statistics are anisotropic with respect to the LOS due to the RSD and the projection of galaxy shape to the sky plane: $\xi_{g\gamma}(\mathbf{r}) = \xi_{g\gamma}(r_p, r_{\parallel})$ and $P_{g\gamma}(\mathbf{k}) = P_{g\gamma}(k_p, k_{\parallel})$, respectively.

The projected correlation function is defined by the integral of the correlation function over the LOS:

$$w_{g\gamma}(r_p; \Pi_{\max}, z) = \int_{-\Pi_{\max}}^{\Pi_{\max}} dr_{\parallel} \xi_{g\gamma}(r_p, r_{\parallel}, z), \quad (\text{A8})$$

where Π_{\max} is the projection length of the LOS direction for which an observer needs to specify; as our default choice, we adopt $\Pi_{\max} = 100 h^{-1}$ Mpc. This expression corresponds to the projected correlation at a single, representative redshift. If we take into account the redshift dependence, we can follow the method in Singh, Mandelbaum & More (2015) as

$$w_{g\gamma}(r_p; \Pi_{\max}, \bar{z}) \equiv \int dz W(z) w_{g\gamma}(r_p; \Pi_{\max}, z), \quad (\text{A9})$$

where $W(z)$ is the redshift distribution of the galaxy density and shape tracers, defined as

$$W(z) = \frac{p_g(z) p_{\gamma}(z)}{\chi^2 d\chi/dz} \left[\int dz \frac{p_g(z) p_{\gamma}(z)}{\chi^2 d\chi/dz} \right]^{-1}. \quad (\text{A10})$$

A2 Expression with spherical Bessel function

To numerically evaluate the correlation function $\xi_{g\gamma}$, one has to compute the transform in equation (A7) from the input model $P_{g\gamma}$. The standard method is to use the isotropy around the LOS on the sky plane and integrate it in the cylindrical coordinates (e.g. Singh, Mandelbaum & More 2015). In this work, we employ the spherical coordinates and use an alternative expression with the spherical Bessel function derived in Kurita & Takada (2022). We here briefly review the derivation.

First, we decompose the model power spectrum into the multipoles of the associated Legendre polynomials with $m = 2, \mathcal{L}_{\ell}^2$, as

$$P_{g\gamma}(k_p, k_{\parallel}) = P_{g\gamma}(k, \mu_{\mathbf{k}}) = \sum_{\ell \geq 2} P_{g\gamma}^{(\ell)}(k) \mathcal{L}_{\ell}^2(\mu_{\mathbf{k}}), \quad (\text{A11})$$

where $\mu_{\mathbf{k}} \equiv \hat{\mathbf{k}} \cdot \hat{\mathbf{n}} = k_{\parallel}/k$ is the cosine between the wave vector and the LOS $\hat{\mathbf{n}}$. Note $\mathcal{L}_2^2(x) = 3(1-x^2)$, $\mathcal{L}_4^2(x) = 15(1-x^2)(7x^2-1)/2$, and so forth. Substituting equation (A11) into equation (A7) and employing the spherical coordinates, we have

$$\xi_{g\gamma}(\mathbf{r}) = \sum_{\ell \geq 2} \int \frac{k^2 dk}{2\pi^2} P_{g\gamma}^{(\ell)}(k) \int \frac{d\Omega_{\mathbf{k}}}{4\pi} \mathcal{L}_{\ell}^2(\mu_{\mathbf{k}}) e^{2i(\phi_{\mathbf{k}} - \phi_r)} e^{i\mathbf{k}\cdot\mathbf{r}}. \quad (\text{A12})$$

Recalling the definition of the spherical harmonics,

$$Y_{\ell}^m(\hat{\mathbf{k}}) = N_{\ell}^m \mathcal{L}_{\ell}^m(\mu_{\mathbf{k}}) e^{im\phi_{\mathbf{k}}}, \quad (\text{A13})$$

with N_{ℓ}^m being the normalization factor

$$N_{\ell}^m = \sqrt{\frac{(2\ell+1)(\ell-m)!}{4\pi(\ell+m)!}}, \quad (\text{A14})$$

and using the plane-wave expansion

$$e^{i\mathbf{k}\cdot\mathbf{r}} = 4\pi \sum_{\ell, m} i^{\ell} j_{\ell}(kr) Y_{\ell}^{m*}(\hat{\mathbf{k}}) Y_{\ell}^m(\hat{\mathbf{r}}), \quad (\text{A15})$$

we carry out the angle average of the wave vector $\hat{\mathbf{k}}$ as

$$\begin{aligned} & \sum_{\ell \geq 2} \int \frac{k^2 dk}{2\pi^2} P_{g\gamma}^{(\ell)}(k) \int \frac{d\Omega_{\mathbf{k}}}{4\pi} \mathcal{L}_{\ell}^2(\mu_{\mathbf{k}}) e^{2i(\phi_{\mathbf{k}} - \phi_r)} e^{i\mathbf{k}\cdot\mathbf{r}} \\ &= \sum_{\ell \geq 2} \int \frac{k^2 dk}{2\pi^2} P_{g\gamma}^{(\ell)}(k) \int \frac{d\Omega_{\mathbf{k}}}{4\pi} (N_{\ell}^2)^{-1} Y_{\ell}^2(\hat{\mathbf{k}}) \\ & \quad \times 4\pi \sum_{\ell', m'} i^{\ell'} j_{\ell'}(kr) Y_{\ell'}^{m'*}(\hat{\mathbf{k}}) Y_{\ell'}^m(\hat{\mathbf{r}}) e^{-2i\phi_r} \\ &= \sum_{\ell \geq 2} i^{\ell} \int \frac{k^2 dk}{2\pi^2} P_{g\gamma}^{(\ell)}(k) j_{\ell}(kr) (N_{\ell}^2)^{-1} Y_{\ell}^2(\hat{\mathbf{r}}) e^{-2i\phi_r} \\ &= \sum_{\ell \geq 2} \left[i^{\ell} \int \frac{k^2 dk}{2\pi^2} P_{g\gamma}^{(\ell)}(k) j_{\ell}(kr) \right] \mathcal{L}_{\ell}^2(\mu_r). \end{aligned} \quad (\text{A16})$$

In the second equation, we have used the orthogonality

$$\int d\Omega_{\mathbf{k}} Y_{\ell}^m(\hat{\mathbf{k}}) Y_{\ell'}^{m'*}(\hat{\mathbf{k}}) = \delta_{\ell\ell'} \delta_{mm'}. \quad (\text{A17})$$

By comparing this result and the multipoles of the correlation function defined by

$$\xi_{g\gamma}(r_p, r_{\parallel}) = \sum_{\ell \geq 2} \xi_{g\gamma}^{(\ell)}(r) \mathcal{L}_{\ell}^2(\mu_r), \quad (\text{A18})$$

where $\mu_r \equiv \hat{\mathbf{r}} \cdot \hat{\mathbf{n}} = r_{\parallel}/r$, we obtain the expression of the multipoles

$$\xi_{g\gamma}^{(\ell)}(r) = i^{\ell} \int \frac{k^2 dk}{2\pi^2} P_{g\gamma}^{(\ell)}(k) j_{\ell}(kr), \quad (\text{A19})$$

which can be computed by the use of FFTlog algorithm (Hamilton 2015).

Let us consider the linear model, i.e. linear alignment model (Hirata & Seljak 2004) with Kaiser formula (Kaiser 1987), as an example. The model power spectrum is given by

$$P_{g\gamma}(k, \mu_{\mathbf{k}}) = \frac{1 - \mu_{\mathbf{k}}^2}{2} (1 + \beta \mu_{\mathbf{k}}^2) b_g b_K P_{\text{mm}}(k), \quad (\text{A20})$$

where $\beta \equiv f/b_g$, P_{mm} is the linear matter power spectrum, b_g and $b_K \equiv -2A_{1A} C_1 \rho_{\text{crit}} \Omega_m / \bar{D}$ are the linear bias of the density sample and

shape bias, respectively. The multipole coefficients of the associated Legendre polynomials then become

$$P_{\text{gy}}^{(2)}(k) = \frac{1}{6} \left(1 + \frac{\beta}{7} \right) b_g b_K P_{\text{mm}}(k), \quad (\text{A21})$$

$$P_{\text{gy}}^{(4)}(k) = \frac{1}{105} \beta b_g b_K P_{\text{mm}}(k), \quad (\text{A22})$$

and zero otherwise. Plugging these into equation (A19), we obtain the multipoles of correlation function with the Hankel transforms of the input matter power spectrum:

$$\xi_{\text{gy}}^{(2)}(r) = \frac{1}{6} \left(1 + \frac{\beta}{7} \right) b_g b_K \xi_{\text{mm}}^{(2)}(r), \quad (\text{A23})$$

$$\xi_{\text{gy}}^{(4)}(r) = \frac{1}{105} \beta b_g b_K \xi_{\text{mm}}^{(4)}(r), \quad (\text{A24})$$

where we have defined the multipoles of matter correlation function:

$$\xi_{\text{mm}}^{(\ell)}(r) \equiv i^\ell \int \frac{k^2 dk}{2\pi^2} P_{\text{mm}}(k) j_\ell(kr). \quad (\text{A25})$$

Once we prepare these multipoles, we can obtain the projected correlation function by integrating over the LOS as in equation (A8),

$$\begin{aligned} w_{\text{gy}}(r_p; \Pi, z) &= \int_{-\Pi_{\text{max}}}^{\Pi_{\text{max}}} dr_{\parallel} \xi_{\text{gy}}(r_p, r_{\parallel}, z) \\ &= \sum_{\ell \geq 2} \int_{-\Pi_{\text{max}}}^{\Pi_{\text{max}}} dr_{\parallel} \xi_{\text{gy}}^{(\ell)}(r) \mathcal{L}_\ell^2(\mu_r), \end{aligned} \quad (\text{A26})$$

$$\text{with } \mu_r = \sqrt{r_{\parallel}^2 / (r_p^2 + r_{\parallel}^2)}.$$

APPENDIX B: IA OF CLUSTERS WITH VARYING SHAPE ESTIMATORS IN MOCK

We checked how different shape estimators affect the measured IA of galaxy clusters in mock simulation. The shape of galaxy clusters are measured using

- (i) dark matter particle distribution (DM),

$$I_{ij} = \frac{\sum_n m_n \frac{x_{ni} x_{nj}}{r_n^2}}{\sum_n m_n}, \quad (\text{B1})$$

where m_n is the mass of the n th particle within the halo, x_{ni}, x_{nj} ($i, j = 1, 2$) are the position coordinates of this particle with respect to the centre of cluster, and r_n is the distance of the particle to the cluster centre;

- (ii) satellite distribution within dark matter haloes (Halo Sat),

$$I_{ij} = \frac{\sum_n x_{ni} x_{nj}}{N_g}, \quad (\text{B2})$$

where x_{ni}, x_{nj} ($i, j = 1, 2$) are the positions of n th satellite galaxy with respect to the centre of cluster, and N_g is the total number of satellite galaxies used for the calculation;

(iii) redMaPPer identified member galaxy distribution (RM Mem), I_{ij} is calculated using equation (B2), except that we use member galaxies identified by the redMaPPer cluster finder;

(iv) redMaPPer identified redMaPPer members that truly belong to the clusters (RM True Mem), also using equation (B2).

Fig. B1 showed that, w_{h+} measured using γ (DM) shows the strongest signal, and satellite distributions trace the DM distribution rather well, showing only a slightly weaker IA signal, as shown by the blue line. This is expected since the satellite galaxies are populated following the dark matter distribution. IA measured using redMaPPer

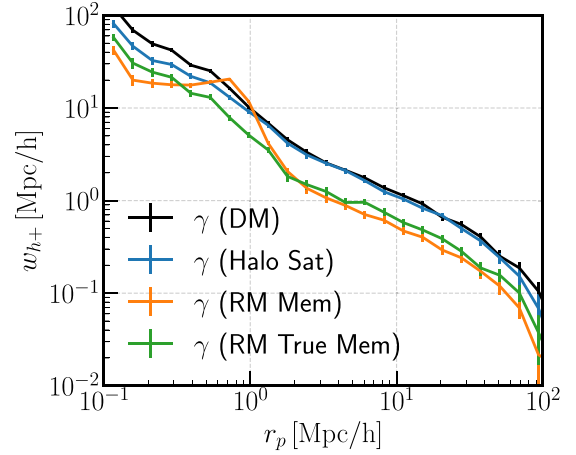


Figure B1. The IA of clusters in the mock clusters ($20 \leq \lambda_{\text{obs}} < 200$), with different shape estimators. The black, blue, orange, and green lines show the measurement using shapes estimated using DM particles, satellites within dark matter haloes, redMaPPer identified cluster members, and true cluster members identified by redMaPPer. Note that here we show the results for one simulation realization; the results are same across all the realizations.

identified member galaxy distribution γ (RM Mem) show the lowest signal, with a bump at $r_p \sim 0.8 h^{-1}$ Mpc. If interlopers are removed for the shape calculation, the bump disappears and the IA signal increases a little bit, shown by the green line. However, the IA signal is still much lower than the one measured using DM and satellite galaxy distribution, indicating that another factor, i.e. the satellites that are missed by redMaPPer algorithm, is also responsible for decreasing the IA signal.

APPENDIX C: CLUSTERS OF VARIOUS RICHNESS BINS IN THE MOCK

Fig. C1 shows the IA of clusters in the mock in various richness bins

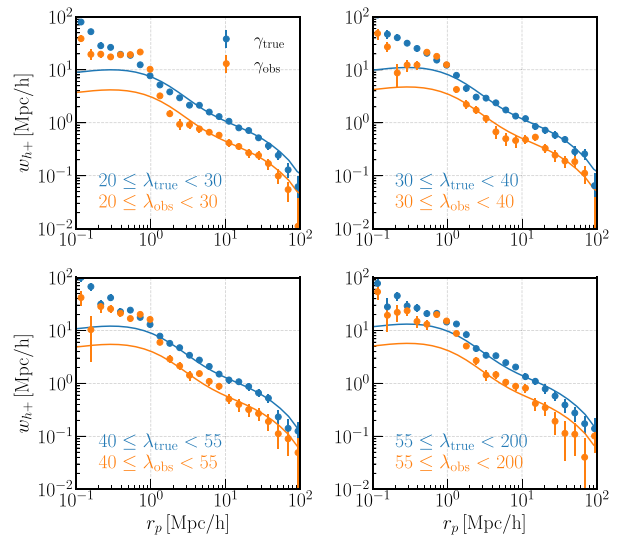


Figure C1. The IA of mock observe (orange) and mock true (blue) clusters, in various richness bins in one simulation realization. The dots are measurement and lines are fitting using NLA in the range of $6 h^{-1}$ Mpc $< r_p < 70 h^{-1}$ Mpc. The error bars are estimated using jackknife subsamples.

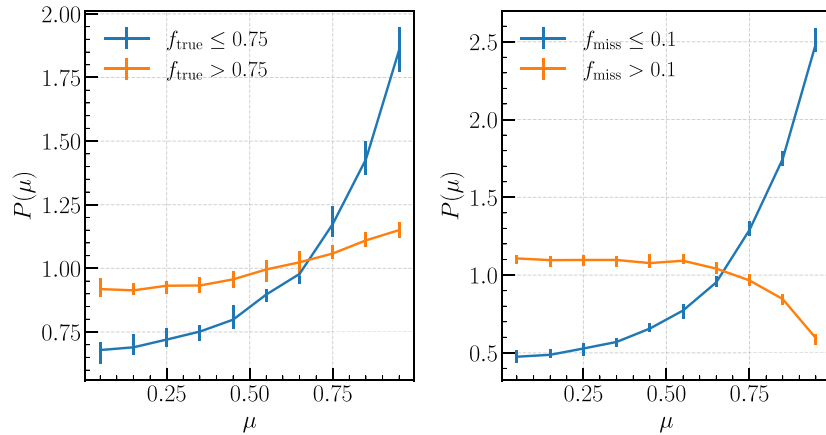


Figure D1. Distribution of cosine of the angle, θ , between major axis of the halo and LOS direction for low/high f_{true} and low/high f_{miss} subsamples with $20 \leq \lambda_{\text{obs}} < 200$. Here $\mu \equiv |\cos \theta|$. The lines are median distribution of 19 realizations, and the error bars show the 1σ dispersion among the realizations.

bins and the corresponding NLA fitting results. The IA signal of mock true samples are obtained by selecting clusters using λ_{true} and measuring shapes γ_{true} using satellites within haloes. The IA signal of mock observe samples are gotten by selecting clusters using λ_{obs} and measuring shapes γ_{obs} using redMaPPer identified cluster members as in observation. The IA of mock observe is lower than that of mock true in all richness bins. The NLA model fits the signal well in the range of $6 h^{-1} \text{Mpc} < r_p < 70 h^{-1} \text{Mpc}$, and the resulting A_{IA} are summarized in Table 1.

APPENDIX D: CLUSTER ORIENTATION AND PROJECTION EFFECTS

Fig. D1 shows the distribution of the orientation of clusters with respect to LOS direction for clusters with lower and higher f_{true} (f_{miss}) separately. The cluster orientation is obtained by calculating the major eigenvectors from the three-dimensional inertia tensor using dark matter particle distribution,

$$I_{ij} = \frac{\sum_n m_n \frac{x_{ni} x_{nj}}{r_n^2}}{\sum_n m_n}, \quad (\text{D1})$$

where x_{ni} , x_{nj} ($i, j = 1, 2, 3$) are the positions of n th particle with respect to the centre of cluster. The angle between major axis of the halo and LOS direction is characterized by $\mu \equiv |\cos \theta|$. Clusters selected using $f_{\text{true}} \leq 0.75$ or $f_{\text{miss}} \leq 0.1$ tend to have their major axis parallel with the LOS direction. On the other hand, clusters with $f_{\text{true}} > 0.75$ do not show a strong orientation preference. Cluster with $f_{\text{miss}} > 0.1$ show a clear tendency of major axis perpendicular to the LOS direction. Fig. D1 shows the distribution for clusters with $20 \leq \lambda_{\text{obs}} < 200$ only. The results stay the same when we use different λ_{obs} ranges.

APPENDIX E: DEPENDENCE ON HALO MASS AND REDSHIFT OF A_{IA}

Fig. E1 shows how A_{IA} varies with halo mass and redshift. The lines are results obtained from simulations, where the halo shapes are measured using equation (B1), the dots with error bars are results

from observation. The halo mass of redMaPPer clusters are obtained using the mass–richness relation from Simet et al. (2017), where

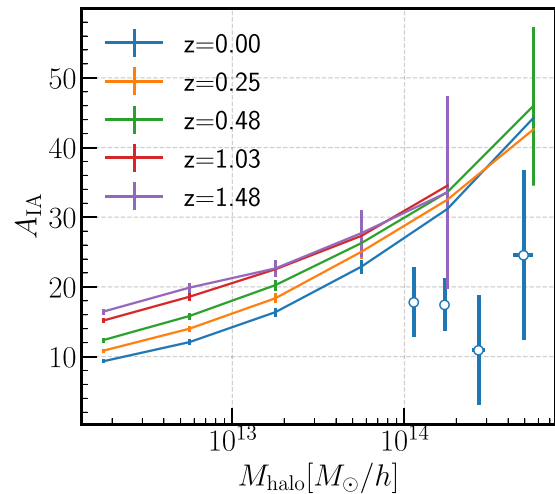


Figure E1. A_{IA} as a function of halo mass and redshift. The lines with error bars are calculated from dark matter haloes in N -body simulation as done in Kurita et al. (2021). The dots are results using SDSS DR8 redMaPPer catalogue.

weak lensing analysis was performed for the redMaPPer clusters at $0.1 < z \leq 0.33$. Simet et al. (2017) parametrized the relation as $M = M_0(\lambda/\lambda_0)^\alpha$, where $\log M_0 = 14.344 \pm 0.031$, $\alpha = 1.33^{+0.09}_{-0.10}$, and $\lambda_0 = 40$. We use the mean richness value of each subsample to do the conversion. The simulation shows that A_{IA} increases with halo mass and redshift. However, the redshift dependence is very weak/almost gone for haloes with $M_h > 10^{14} h^{-1} M_\odot$. The observed $A_{\text{IA}}-M_h$ relation is clearly much lower than that from dark matter halo simulation, which is mainly due to the projection effects.

This paper has been typeset from a $\text{\TeX}/\text{\LaTeX}$ file prepared by the author.